

# Journal of Astronomical Telescopes, Instruments, and Systems

AstronomicalTelescopes.SPIEDigitalLibrary.org

## Hard x-ray imager onboard Hitomi (ASTRO-H)

Kazuhiro Nakazawa  
Goro Sato  
Motohide Kokubun  
Teruaki Enoto  
Yasushi Fukazawa  
Kouichi Hagino  
Katsuhiro Hayashi  
Jun Kataoka  
Junichiro Katsuta  
Shogo B. Kobayashi  
Philippe Laurent  
Francois Lebrun  
Olivier Limousin  
Daniel Maier  
Kazuo Makishima  
Tsunefumi Mizuno  
Kunishiro Mori  
Takeshi Nakamori  
Toshio Nakano

Hirofumi Noda  
Hirokazu Odaka  
Masanori Ohno  
Masayuki Ohta  
Shinya Saito  
Rie Sato  
Hiroyasu Tajima  
Hiromitsu Takahashi  
Tadayuki Takahashi  
Shin'ichiro Takeda  
Takaaki Tanaka  
Yukikatsu Terada  
Hideki Uchiyama  
Yasunobu Uchiyama  
Shin Watanabe  
Kazutaka Yamaoka  
Yoichi Yatsu  
Takayuki Yuasa

Kazuhiro Nakazawa, Goro Sato, Motohide Kokubun, Teruaki Enoto, Yasushi Fukazawa, Kouichi Hagino, Katsuhiro Hayashi, Jun Kataoka, Junichiro Katsuta, Shogo B. Kobayashi, Philippe Laurent, Francois Lebrun, Olivier Limousin, Daniel Maier, Kazuo Makishima, Tsunefumi Mizuno, Kunishiro Mori, Takeshi Nakamori, Toshio Nakano, Hirofumi Noda, Hirokazu Odaka, Masanori Ohno, Masayuki Ohta, Shinya Saito, Rie Sato, Hiroyasu Tajima, Hiromitsu Takahashi, Tadayuki Takahashi, Shin'ichiro Takeda, Takaaki Tanaka, Yukikatsu Terada, Hideki Uchiyama, Yasunobu Uchiyama, Shin Watanabe, Kazutaka Yamaoka, Yoichi Yatsu, Takayuki Yuasa, "Hard x-ray imager onboard Hitomi (ASTRO-H)," *J. Astron. Telesc. Instrum. Syst.* 4(2), 021410 (2018), doi: 10.1117/1.JATIS.4.2.021410.

# Hard x-ray imager onboard Hitomi (ASTRO-H)

Kazuhiro Nakazawa,<sup>a,b,\*†</sup> Goro Sato,<sup>c</sup> Motohide Kokubun,<sup>c</sup> Teruaki Enoto,<sup>d,e</sup> Yasushi Fukazawa,<sup>f</sup> Kouichi Hagino,<sup>g</sup> Katsuhiro Hayashi,<sup>c,h</sup> Jun Kataoka,<sup>i</sup> Junichiro Katsuta,<sup>f</sup> Shogo B. Kobayashi,<sup>j</sup> Philippe Laurent,<sup>k,l</sup> Francois Lebrun,<sup>k</sup> Olivier Limousin,<sup>l</sup> Daniel Maier,<sup>l</sup> Kazuo Makishima,<sup>m</sup> Tsunefumi Mizuno,<sup>f,n</sup> Kunishiro Mori,<sup>c</sup> Takeshi Nakamori,<sup>o</sup> Toshio Nakano,<sup>p</sup> Hirofumi Noda,<sup>q,r</sup> Hirokazu Odaka,<sup>s</sup> Masanori Ohno,<sup>f</sup> Masayuki Ohta,<sup>c</sup> Shinya Saito,<sup>t</sup> Rie Sato,<sup>c</sup> Hiroyasu Tajima,<sup>u</sup> Hiromitsu Takahashi,<sup>f</sup> Tadayuki Takahashi,<sup>c</sup> Shin'ichiro Takeda,<sup>v</sup> Takaaki Tanaka,<sup>j</sup> Yukikatsu Terada,<sup>w</sup> Hideki Uchiyama,<sup>x</sup> Yasunobu Uchiyama,<sup>t</sup> Shin Watanabe,<sup>c</sup> Kazutaka Yamaoka,<sup>h,u</sup> Yoichi Yatsu,<sup>y</sup> and Takayuki Yuasa<sup>m</sup>

<sup>a</sup>The University of Tokyo, Department of Physics, Tokyo, Japan

<sup>b</sup>The University of Tokyo, Research Center for the Early Universe, School of Science, Tokyo, Japan

<sup>c</sup>Japan Aerospace Exploration Agency, Institute of Space and Astronautical Science, Sagami-hara, Kanagawa, Japan

<sup>d</sup>Kyoto University, Department of Astronomy, Kyoto, Japan

<sup>e</sup>Kyoto University, The Hakubi Center for Advanced Research, Kyoto, Japan

<sup>f</sup>Hiroshima University, School of Science, Higashi-Hiroshima, Japan

<sup>g</sup>Tokyo University of Science, Department of Physics, Yamazaki, Noda, Chiba, Japan

<sup>h</sup>Nagoya University, Department of Physics, Nagoya, Aichi, Japan

<sup>i</sup>Waseda University, Research Institute for Science and Engineering, Shinjuku, Tokyo, Japan

<sup>j</sup>Kyoto University, Department of Physics, Sakyo, Kyoto, Japan

<sup>k</sup>Laboratoire APC, Paris, France

<sup>l</sup>CEA Saclay, Gif sur Yvette, France

<sup>m</sup>Institute of Physical and Chemical Research, Wako, Saitama, Japan

<sup>n</sup>Hiroshima University, Hiroshima Astrophysical Science Center, Hiroshima, Japan

<sup>o</sup>Yamagata University, Faculty of Science, Yamagata, Japan

<sup>p</sup>RIKEN Nishina Center, Wako, Saitama, Japan

<sup>q</sup>Tohoku University, Frontier Research Institute for Interdisciplinary Sciences, Sendai, Miyagi, Japan

<sup>r</sup>Tohoku University, Astronomical Institute, Sendai, Miyagi, Japan

<sup>s</sup>Stanford University, Kavli Institute for Particle Astrophysics and Cosmology, Stanford, California, United States

<sup>t</sup>Rikkyo University, Department of Physics, Tokyo, Japan

<sup>u</sup>Nagoya University, Institute for Space-Earth Environmental Research, Nagoya, Aichi, Japan

<sup>v</sup>Okinawa Institute of Science and Technology Graduate University, Okinawa, Japan

<sup>w</sup>Saitama University, Department of Physics, Saitama, Japan

<sup>x</sup>Shizuoka University, Faculty of Education, Shizuoka, Japan

<sup>y</sup>Tokyo Institute of Technology, Department of Physics, Tokyo, Japan

**Abstract.** The hard x-ray imaging spectroscopy system of “Hitomi” x-ray observatory is composed of two sets of hard x-ray imagers (HXI) coupled with hard x-ray telescopes (HXT). With a 12-m focal length, the system provides fine (1'.7 half-power diameter) imaging spectroscopy covering about 5 to 80 keV. The HXI sensor consists of a camera, which is composed of four layers of Si and one layer of CdTe semiconductor imagers, and an active shield composed of nine Bi<sub>4</sub>Ge<sub>3</sub>O<sub>12</sub> scintillators to provide low background. The two HXIs started observation on March 8 and 14, 2016 and were operational until 26 March. Using a Crab observation, 5 to 80 keV energy coverage and good detection efficiency were confirmed. The detector background level of 1 to  $3 \times 10^{-4}$  counts s<sup>-1</sup> keV<sup>-1</sup> cm<sup>-2</sup> (in detector geometrical area) at 5 to 80 keV was achieved, by cutting the high-background time-intervals, adopting sophisticated energy-dependent imager layer selection, and baffling of the cosmic x-ray background and active-shielding. This level is among the lowest of detectors working in this energy band. By comparing the effective area and the background, it was shown that the HXI had a sensitivity that is same to that of NuSTAR for point sources and 3 to 4 times better for largely extended diffuse sources. © The Authors. Published by SPIE under a Creative Commons Attribution 3.0 Unported License. Distribution or reproduction of this work in whole or in part requires full attribution of the original publication, including its DOI. [DOI: [10.1117/1.JATIS.4.2.021410](https://doi.org/10.1117/1.JATIS.4.2.021410)]

Keywords: gamma rays; x-rays; detectors; satellites; astronomy.

Paper 17058SSP received Aug. 7, 2017; accepted for publication Mar. 9, 2018; published online Apr. 9, 2018.

## 1 Introduction

The x-ray observatory “Hitomi” was a mission led by JAXA, in collaboration with NASA, ESA, SRON, Canadian Space Agency (CSA), and many other research institutes and universities.<sup>1,2</sup>

It was designed to carry out high-resolution x-ray spectroscopy with nondispersive spectrometer in 0.3 to 12 keV, as well as

wideband high-sensitivity spectroscopy with imaging up to 80 keV and without imaging up to 600 keV. The former can diagnose the temperature, ionization state, and dynamical motion of celestial plasma, and the latter can distinguish hot-thermal and nonthermal emission from the main thermal component. The combination of these two characteristics is the key to understanding how the kinetic energy within hot plasma is converted into heat and particle acceleration in the universe.

The hard x-ray imaging spectroscopy is provided by two hard x-ray imagers (HXI), which is the main scope of this paper, coupled with two hard x-ray telescopes (HXT).<sup>3</sup> The

\*Address all correspondence to: Kazuhiro Nakazawa, E-mail: [nakazawa@u.phys.nagoya-u.ac.jp](mailto:nakazawa@u.phys.nagoya-u.ac.jp)

†Now moved to Nagoya University.

system covers the energy band from 5 to 80 keV, with  $1'.7$  half-power diameter (HPD) angular resolution. The HXI is based on a set of technologies specifically developed. The imagers are made from double-sided Si strip detectors (DSSD)<sup>4,5</sup> and a newly developed CdTe double-sided strip detector (CdTe-DSD),<sup>6</sup> coupled to specifically developed low-noise analog application-specific integrated circuit (ASIC).<sup>7</sup> The HXI also adopts the low background technology verified by the hard x-ray detector (HXD)<sup>8,9</sup> onboard the “Suzaku” satellite, in particular the well-shaped-thick active-shield to realize low background.<sup>10</sup> The HXT employs a newly developed multilayer super mirror optics. It accumulates hard x-ray photons into the low background imager, and improves the sensitivity by  $\sim 100$  times compared with its predecessor, the HXD.

**Table 1** Specification of the HXI + HXT system.

Angular resolution	$1'.7$ @30 keV HPD
Focal length	12 m ( $1' = 3.5$ mm)
FoV	$9'.17 \times 9'.17$ ( $32 \times 32$ mm <sup>2</sup> )
Effective area	$\sim 300$ cm <sup>2</sup> @ 30 keV (HXI1 and 2 summed)
Energy band	5 to 80 keV
Energy resolution	1.0 and 2.0 keV (FWHM) @10 and 60 keV, respectively
Time resolution	25.6 $\mu$ s (relative)

Hitomi was launched on February 17, 2016, into a low Earth orbit with an altitude of 575 km and an inclination of 31 deg. After the start-up operations, several celestial objects were observed before the mission was lost on March 26. The scientific results are published elsewhere, including those using the HXI data, such as IGR J16318–4848, G21.5–0.9, and Crab. We summarize the HXI hardware design, logs of the commissioning operation, and brief review of the in-orbit performance. Detail of the in-orbit performance and instrument response is reported in Hagino et al.<sup>11</sup>

## 2 Hard X-Ray Imagers Design

### 2.1 Overall Design

Combined with the HXT located 12-m apart, the HXI provides imaging spectroscopy in the 5- to 80-keV energy band with a  $9'.17 \times 9'.17$  field of view (FoV) by utilizing an imager with  $32 \times 32$  mm<sup>2</sup> detection area. Energy resolution better than 2.0 keV in full width at half maximum (FWHM) at 30 keV is also required to resolve activation lines and discard these energy bands if needed. Specification of the hard x-ray imaging spectroscopy system is summarized in Table 1 and their arrangement on the satellite is shown in Fig. 1. The Hitomi satellite consists of a main body and a plate, which carries two HXI sensor parts, called the HXI plate. It is connected to the satellite base via the extensible optical bench (EOB), which extends by 6 m in orbit. At the satellite main body, the fixed optical bench (FOB) is installed, and the two HXTs (along with other two x-ray mirrors for the soft x-ray instruments) are mounted on its top plate.

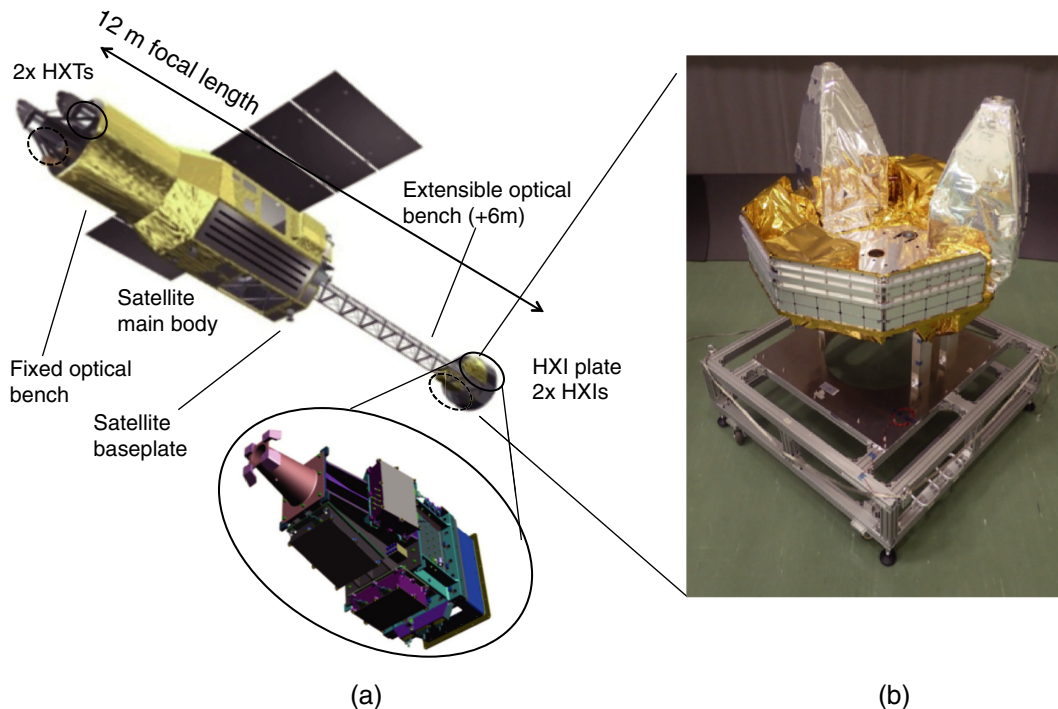


**Fig. 1** (a) The hard x-ray imaging spectroscopy system of Hitomi. The two HXI-Ss are located on the HXI plate, connected to the satellite main body via the EOB. (b) Photo of the HXI plate equipped with two HXI-S covered with thermal blankets. Also seen in front is the radiator used to cool the HXI base plates.

The HXI utilizes the satellite body and the FOB structure as baffles to stop the Cosmic x-ray background (CXB) directly reaching the HXI, not focused by the HXT. In the middle of the FOB, 0.5-mm-thick Sn sheets are glued around the two optical openings on a plate. At the bottom of the satellite baseplate, 0.3-mm-thick Pb sheets are glued surrounding the optical openings for the two HXIs, covering almost  $1 \times 1 \text{ m}^2$  individually. (Some areas covered with thick structures, such as the dewar of the soft x-ray spectrometer, are not covered by the Pb sheet to reduce total weight.) The HXT themselves have precollimators to stop stray light and also a Pb sheet to fill the central opening. Using these Pb/Sn sheets and with baffles within the HXI itself (see Sec. 2.2.1), the CXB leakage to the HXI system is kept negligible compared with the non-x-ray background (NXB).

The two HXI systems are named as HXI1 and HXI2. As shown in Fig. 2, each system is composed of four modules, the sensor part HXI-S, the analog and power control electronics box HXI-AE (analog electronics), the digital logic box using FPGA (field programmable gate array) HXI-DPU (data processing unit), and the CPU box HXI-DE (digital electronics).<sup>12</sup> All boxes other than the two HXI-DE are located on the HXI plate. The base of each HXI-S is mounted on the HXI cold-plate, thermally connected via heat pipes to the HXI radiator. Heaters attached to heat-pipes, electronics boxes, and the cold plates are controlled by another electronics box named HXI-HCE (heater control electronics). The two HXI-DE (HXI1-DE and HXI2-DE) are mounted on the side-panels of the satellite main body. Two sets of SpaceWire cables and power lines are connected to the HXI plate, extending by 6 m along with the EOB in orbit. All electric powers of HXI-S, AE, and DPU are provided from the power supply board (DC/DC converters) in HXI-DPU, whereas HXI-HCE and the two HXI-DE boxes have their own power supply boards.

## 2.2 Design of HXI-S

### 2.2.1 Overview

As shown in Fig. 3, HXI-S consists of the HXI camera part and the active shield part. The former includes four layers of DSSDs and a CdTe-DSD imagers, whereas the latter is composed of nine active shield units made of large  $\text{Bi}_4\text{Ge}_3\text{O}_{12}$  (BGO) scintillator crystals individually coupled to avalanche photo diodes (APD),<sup>13</sup> and the housing structure made of carbon-fiber-reinforced plastic (CFRP) to mechanically hold them. The DSSD and APD are purchased from Hamamatsu Photonics, the CdTe-DSD is from Acrorad, and the BGO is from Nikolaev Institute of Inorganic Chemistry.

Right above the imager at the edge of the FoV, a calibration source is located, which is made of an  $^{241}\text{Am}$ -doped plastic scintillator coupled to an APD. Another APD without a scintillator is located near the  $^{241}\text{Am}$  source, to monitor the cosmic-ray (CR) flux within the active shield. CSA and high-voltage (HV) supplies for the APD are placed in two APD-CSA boxes attached to the housing. An APD-CSA box covers seven channels (four side and one bottom BGO units, and the  $^{241}\text{Am}$  and the CR-monitor APDs) and the other covers four channels (four top BGO units). Another box containing two HV suppliers, one for the DSSDs and the other for the CdTe-DSD, called the HV box is also attached. All the HV power supplies are provided from a company SITAEL S.P.A.

HXI-S has a weight of 41.8 kg and a height of 65 cm (see Fig. 3). Structurally, the HXI camera, the bottom BGO unit, and the CFRP housing holding the other eight BGO units are mounted on the base plate made of Al-alloy. In other words, the three components are mechanically and thermally almost isolated to make the development work easy.

Because the HXI utilizes semiconductor imagers (DSSD and CdTe-DSD) and APD, the HXI cold plate is cooled down to

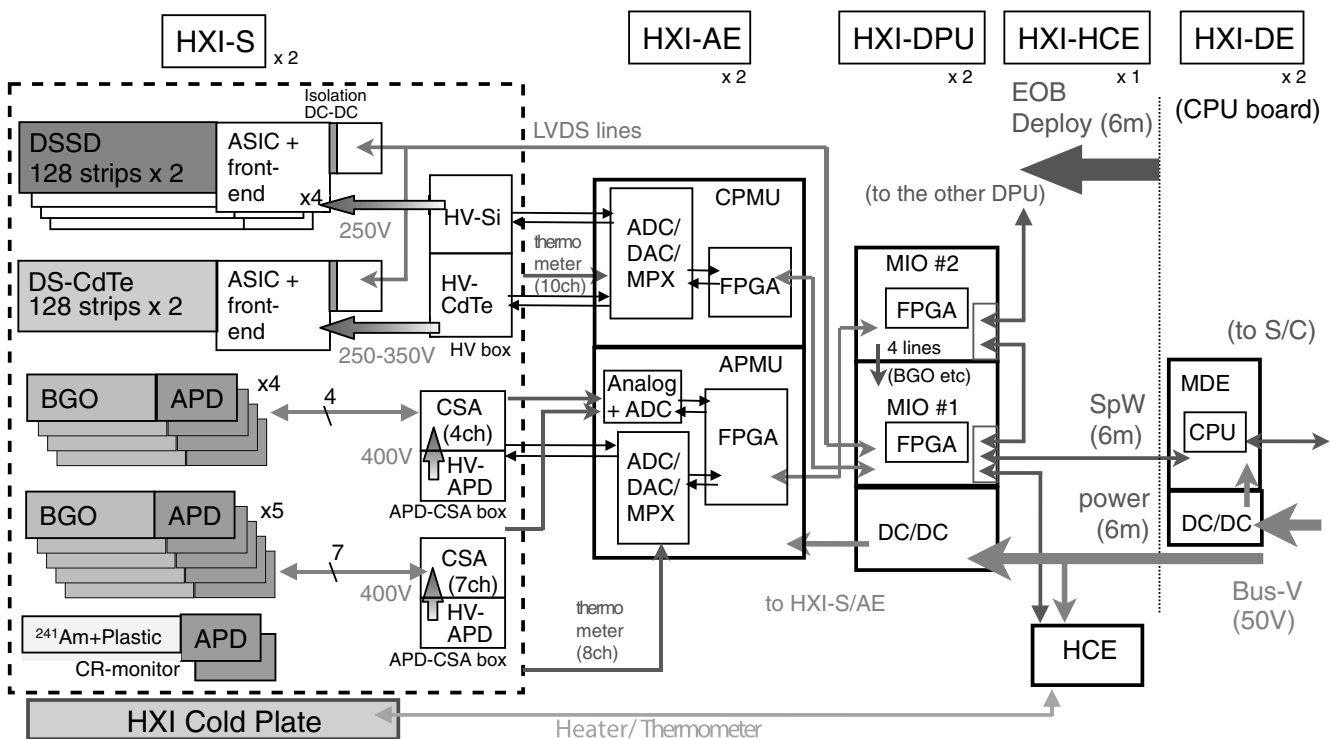
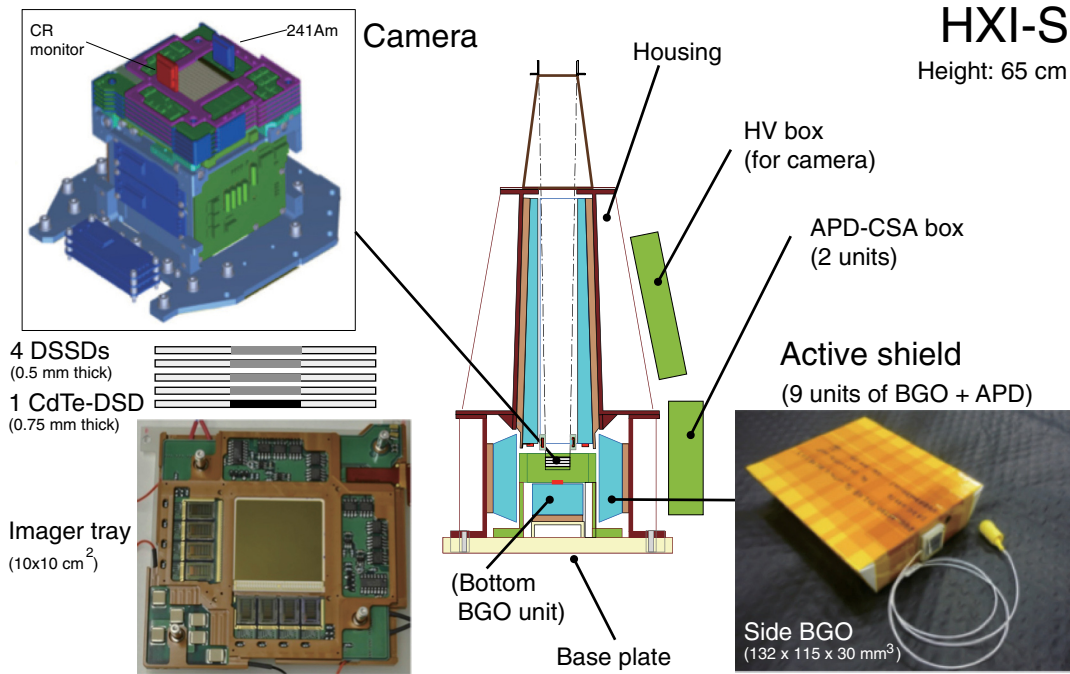


Fig. 2 Block diagram of the HXI subsystem.



**Fig. 3** Overview of HXI-S, composed of a camera, nine active shields, and the housing structure, mounted on the base plate.

$-25^{\circ}\text{C}$  in orbit and controlled within  $\pm 1^{\circ}\text{C}$  using attached heaters. Even though the temperature at the bottom of the HXI-S is thus controlled well, it is exposed to the Sun when the satellite is in the day side, and the heat transfer along the housing structure causes internal temperature gradients. It can be a problem especially in the top BGO units, the most distant from the cold plate because gain of the APDs is sensitive to temperature (typically  $-3\%/^{\circ}\text{C}$  gain variation). To relax this issue, graphite sheets are taped on the surface of the CFRP housing to enhance its thermal conductivity. Outside the HXI-S housing, there are 14 CFRP plates almost completely covering HXI-S to reduce thermal coupling from outside. The plates are held with arms made of glass-fiber-reinforced plastic that has low thermal conductivity. Both inside and outside of the plates are covered with multilayer insulators (MLI) to suppress the radiation heat transfer. Outermost layer of the outside MLI is made of an Ag back-coated teflon sheet to effectively reflect the sunlight as well as to radiate the heat into the sky. Overall, all the APD and camera temperature were controlled within  $\pm 2^{\circ}\text{C}$  in orbit, consistent with preflight estimation. Careful thermal design was also performed in the camera part, to keep the imagers' temperature lower than  $-15^{\circ}\text{C}$  when the HXI cold plate is controlled at  $-25^{\circ}\text{C}$ , see Noda et al.<sup>14</sup> for detail. There is a 15.5-cm-tall baffle structure at the top of HXI-S, which is internally covered with 0.3-mm Pb sheet to stop the CXB coming directly (not through the HXT FoV) into the imager. The Pb sheet was originally designed to be plated on the outside surface of the baffle for easy manufacturing. Monte Carlo simulation performed in the design phase showed that CXB photons coming from the opening window and reaching the inside of the baffle structure are scattered off by the internal CFRP, which is mostly made of elements lighter than carbon, and become a major contributor to the imager background. Thus, the Pb sheet was relocated inside.

The opening of the CXB baffle is the optical axis of the instrument and is covered with the entrance window made of two layers of 30- $\mu\text{m}$ -thick poly-carbonate sheets, with Al

sputtered to the both sides (i.e., four layers of Al in total). The thickness of an Al layer is designed to be 150-nm each. As the window is directly illuminated with sunlight, the light leakage was carefully measured. Originally, it was a single-layer sheet with both sides of Al sputtered, but we found the leak is not negligible, and thus decided to make it double. After the acoustic shock and vibration tests, as well as the light leak test, the double sheet design was finally adopted.

### 2.2.2 Camera part

Design of the camera part is roughly shown in the left panel of Fig. 3 and well reported in Sato et al.<sup>15</sup> The top four layers, namely layers 0, 1, 2, and 3, are made of 0.5-mm-thick DSSDs covering from 5 to about 30 keV, and the last one, layer 4, is made up of 0.75-mm-thick CdTe-DSD covering from about 30 to 80 keV. Both detectors have 250- $\mu\text{m}$  pitch strips in both surfaces, orthogonally oriented to provide two-dimensional position sensitivity. Each side has 128 strips, covering 32- $\times$ 32- $\text{mm}^2$  area. Each strip electrode of the DSSD, in both sides, has a width of 150  $\mu\text{m}$  with a 100- $\mu\text{m}$ -wide gap. Some fraction of photons absorbed in the gap is detected as a “split event,” with signals recorded in two adjacent strips (see Hagino et al.<sup>11</sup> for detail). The strip electrodes of the CdTe-DSD have a width of 230  $\mu\text{m}$  with a 20- $\mu\text{m}$ -wide gap in both sides. The die sizes of both detectors are 34.0  $\times$  34.0  $\text{mm}^2$ . The top side (toward the entrance window) of a DSSD is the *p*-electrode biased to the ground level, and the bottom side is the *n*-electrode biased to  $\sim +250$  V. Similarly, the top side of a CdTe-DSD is the Pt-electrode, and the other side is the Al-electrode biased to +250 to 350 V.

The DSSDs and the CdTe-DSD are mounted on 100- $\times$ 100- $\text{mm}^2$  trays, stacked in 4-mm distance individually. Focal point of the HXT is set at the top layer DSSD (layer 0), located  $\sim 16.5$  mm above the CdTe-DSD. The 12-m-long focal length and 45-cm diameter of the HXT make the defocusing effect in the last CdTe layer  $< 0'.17$ , which is small compared with the 1'.7 HPD.

Each tray is electrically divided into two parts, for top- and bottom-side readout. Each side has four 32-ch low-noise analog ASICs with ADC. The ASIC is named VATA-HXI and was developed in collaboration with IDEAS.<sup>7</sup> ASIC inputs are directly connected to the detector strip electrodes using either wire bonding (DSSD) or combining wire bonding and bump bonding (CdTe-DSD). The bias voltage is applied by floating the common level of the whole circuits handling  $n$ -side (or Al-side) strips by +250 to 350 V. All digital signals are decoupled using magnetic couplers. The power-lines are also generated via isolated DC/DC converters.

Logical “or” of the trigger outputs of four ASICs in  $p$ - and  $n$ -sides of each tray individually are sent to HXI-DPU that sends back sample-and-hold control signal and ADC control signals after specified time intervals. The control signals are shared within all five trays (=10 sides) to synchronize the data acquisition activities. All 1280-ch analog outputs are converted simultaneously by Wilkinson-type ADCs following the individual triggers, whereas only channels with value exceeding the predefined digital value “DTHR” are read out (so-called, a sparse data scan). In addition, the median value (16th highest among the 32 channels each) of the corresponding ASIC is attached to be used to monitor the common mode noise, which is subtracted from individual signals in the on-ground analysis procedure. This approach is optimized for low-noise readout and not for high speed. Nonetheless, the system still is capable to handle trigger rate largely exceeding 1000 Hz, meeting the requirement to observe a source “brighter than the Crab nebula.”

The five-layer imager design is adopted to provide “depth sensing” information to further reduce the detector background.<sup>16</sup> For example, photons with energy below  $\sim 15$  keV are almost completely absorbed in layer 0 (the top layer DSSD), and any signals generated in the other four layers with energy below  $\sim 15$  keV are background. Therefore, selecting only layer 0 for the lowest energy end is the best approach to achieve high sensitivity. In contrast, above  $\sim 30$  keV, most of the photons penetrate all the four layers of DSSDs and are absorbed in the CdTe-DSD, and thus we need to use it. The energy band of each layer is optimized after obtaining the in-orbit background data, as reported in Sec. 3.2 and also in Hagino et al.<sup>11</sup>

The signal information of x-ray photons is recorded event by event. The data packet is composed of the header part with trigger time, event sequence number, trigger patterns, flags (including those from active shields), and other miscellaneous information, followed by the ASIC part containing information from selected ADCs (including the channel IDs and the common mode noise level). In normal operation, only triggers from  $p$ -side of DSSDs and Pt-side of CdTe-DSD are utilized. A typical x-ray event has two signals from one imager, one in the  $p$ -side (or Pt-side) and the other in the  $n$ -side (or Al-side), representing  $Y$ - and  $X$ -positions in raw detector coordinate (RAWY and X), respectively. Compton scattering, interstrip charge sharing, CR penetration, and other secondary interactions within the detector generate more signals. Pulse heights of both sides are used to identify position and qualify the validity of the event (i.e., the two values shall be the same). However, for spectroscopy we only use the pulse height of the  $p$ -side in the DSSDs because that of  $n$ -side has larger noise level caused by the difference in the strip electrode implementation. In CdTe-DSD, slow mobility and short lifetime of the holes degrade the Pt-side spectra, and therefore we use those obtained from the Al-side.

Timing information of each event has a resolution of  $25.6 \mu\text{s}$ . Design and verification of the time-tagging system, not only for the HXI but also including the whole satellite mission systems are summarized in a separate paper.<sup>17</sup>

### 2.2.3 Active-shield and related parts

The background shielding of the HXI combines both passive and active measures. First of all, the flux of the CXB and the Earth albedo gamma-rays (above  $\sim 200$  keV) are strong and shall be baffled as much as possible. CR particles both trapped ( $E \sim 100$  MeV) in the South Atlantic anomaly (SAA) and directly coming from the outer space ( $E \gtrsim 4$  GeV) generate signals in the imager not only when they directly hit it but also from secondary particles and x-rays generated in the baffling/shielding structures. Both prompt and delayed (activation) signals are generated from these particles. The well-shaped active shield design adopted in the HXI is based on the successful heritage from Suzaku HXD,<sup>8,18</sup> to suppress background signals from all these sources.

The active shield made of BGO crystals is forming a well-like shape and is designed to stop or tag gamma-rays (e.g., by identifying Compton scattered events) and CR particles from almost  $4\pi$  direction. In Fig. 4, the geometry of the nine BGO units is presented. There are four top BGO units (ID 1 to 4 in the telemetry data), one bottom unit [ID 7 (ID 5 and 6 are used for the <sup>241</sup>Am source and the CR-monitor.)] and four side units (ID 8 to 11), respectively. Each unit has a typical thickness of  $\sim 3$  cm to passively stop protons with energy  $< \sim 100$  MeV, mostly in the SAA, so that the semiconductor imagers, especially CdTe-DSD, experience less activation. The thickness is also important to provide good interaction probability for activation-induced gamma rays, in particular 511-keV photons from  $\beta^+$  decays.

Each BGO scintillator is glued by an elastic adhesive to a dedicated fiber-reinforced plastic (FRP) plate (using both carbon and glass fibers) through a white paint made of BaSO<sub>4</sub> reflector. The FRP plate is specifically designed to have a thermal expansion rate similar to that of the BGO. The other five surfaces of the scintillator are covered with reflector sheets, the enhanced specular reflector (ESR) from 3M, and a GoreTex sheet. The APD is glued on the BGO’s smallest-area surface to keep the light accumulation efficiency as high as possible<sup>19</sup> in the top and side units. As the bottom BGO is almost cubic, the APD is glued on the top surface for simplicity. Each BGO unit is fixed to the CFRP housing via the mechanical interface of the FRP plate. Small 3- to 4-mm gaps between the BGO crystals are unavoidable for manufacturing. Orientation of these gaps is carefully designed to avoid direct leak of the CXB into the imagers, but the Monte Carlo simulation revealed that the CXB photons scattered within HXI-S will result in non-negligible increase in detector background. Thus, we covered those gaps by taping 0.3-mm-thick Pb sheets on the housing structure.

Each APD has an entrance window with a size of  $10 \times 10 \text{ mm}^2$ , optically connected to the BGO crystal via a silicone adhesive. Signals from the 11 APDs are fed into the two APD-CSA boxes, which are also providing the bias voltage of the APDs. Outputs from the APD-CSA boxes are processed by the APD processing and management unit (APMU) in the HXI-AE box. Detail of the readout electronics is summarized in Ohno et al.<sup>20</sup> The APMU output is connected to HXI-DPU and provides four signal lines to the camera control logic. One line is used to provide a signal within  $5 \mu\text{s}$  from the detection of the BGO signal, which can either be used to veto AD conversion of

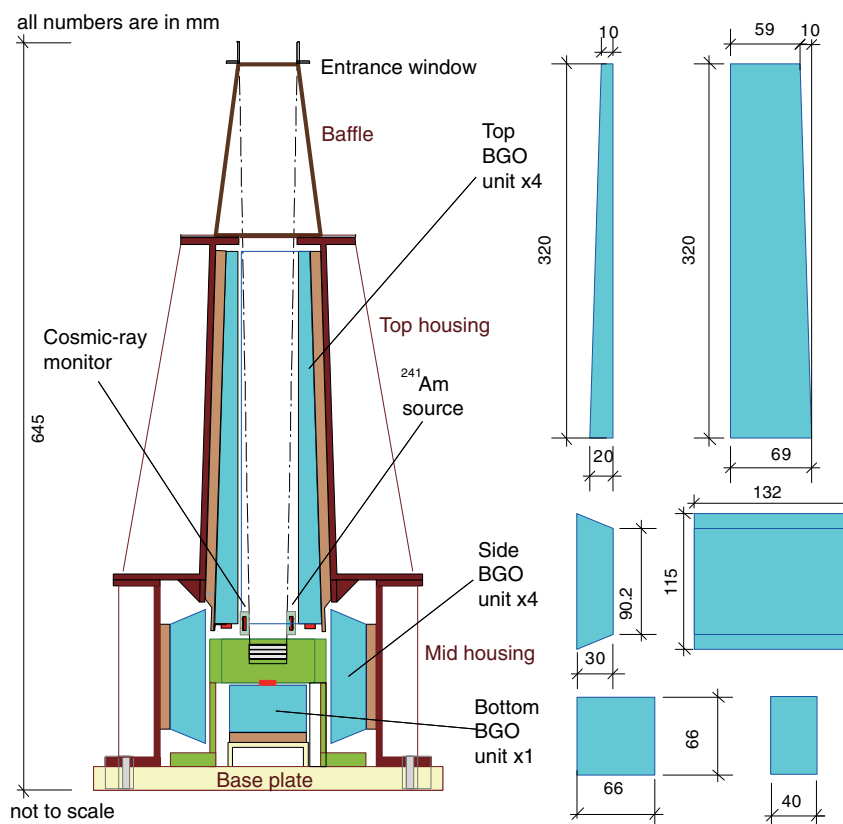


Fig. 4 BGO units and mechanical structures of HXI-S.

the camera to reduce dead time or just be recorded as “fast BGO” flag in the imager event data. Another one tags high-energy deposit events (upper discriminators) representing the time interval in which the CSA of the APD is saturated (the second bit of the “fast BGO” flag). The third one is similar to the “fast BGO” flag, but providing the signal 37 to 42  $\mu\text{s}$  later, using sophisticated filter with much lower energy threshold and is recorded as “HITPAT BGO” flags in the event data.

The final (fourth) line is used for the  $^{241}\text{Am}$  source. Output signals in the APD, originating from  $\alpha$  particles from  $^{241}\text{Am}$  captured in the plastic scintillator are sent to the camera control logic and recorded as “ $^{241}\text{Am}$ ” flag, as the second bit of the “HITPAT BGO” flags. Long-term stability of the imager gain is monitored using the x-ray and gamma-ray lines from this isotope. The  $^{241}\text{Am}$  source is provided by CEA-Sakley and has a decay rate as low as  $\sim 4$  Bq, which is designed to provide better than 1% statistical accuracy of gain monitoring in individual strips every 14 days. As the decay rate is low, the HXI sensitivity will not significantly degrade even if the APD does not work properly in orbit.

The APMU is counting the trigger rate and accumulating the spectra of all 11 APDs; the nine BGO units, the  $^{241}\text{Am}$  source, and the CR-monitor. Because of the limit in the satellite data recorder size, the APD spectra are recorded only 10 min after every SAA passage, and used to calibrate the APD signal gains.

### 3 Commissioning Operation

#### 3.1 Operation Log

A summary of the HXI commissioning operation is shown in Table 2. After the EOB deployment on February 27, 2016,

we kept the HXI-S temperature at 5°C for several hours using the heaters. This operation confirms one of our requirements, which is to be able to “heat-up” the two HXI-S to this temperature. Then, we turned on all the electronics boxes’

Table 2 Logs of the major operations in the HXI start-up phase, in February to March 2016.

Date	Items
February 17	Hitomi launch
	HXI-S temperature set to 5°C
February 27	EOB deployment
February 29	HXI-DPU, AE power on
March 2 to 8	HXI-S cool down operation (to $-25^\circ\text{C}$ )
March 8 to 12	HXI1-S turn on operation
March 12 to 14	HXI2-S turn on operation <sup>a</sup>
March 14	HXI1/2-S observations start at normal conditions
March 19 to 23	G21.5–0.9 first light of the HXI
March 24	ASIC ADC digital threshold (“DTHR”) update
March 25	Crab observation
March 26	Hitomi loss incident

<sup>a</sup>HXI1 observed IGR J16318–4848 for a short period.

**Table 3** HV bias settings of the HXI.

	HXI-1S (V)	HXI-2S (V)
DSSD bias	250	250
CdTe bias	250	350
APD bias		
(four top BGO units)	393	394
(the other seven channels)	400	410

power (HXI-DE, DPU, and AE) to monitor all (18 ch each) thermometers attached to the HXI-S housing structures and cameras. Then, we gradually decreased the heater power of the HXI cold plate to cool it down to our operation temperature of  $-25^{\circ}\text{C}$ .

From March 8, we start turning on the power of the HXI1-S' camera, the two APD-CSA boxes, and the HV box, and gradually increased their bias voltages with a step as small as 100 V per operation. The bias voltage reached the planned value on March 12 as shown in Table 3. Basic data checking showed no performance degradation in orbit (see Sec. 3.2), and we safely started the observation with HXI1. Then, we proceeded with HXI2, which started observation on March 14. Operation parameters were kept unchanged until March 26, except for the ASIC ADC digital thresholds (“DTHR”), which were increased to reduce the data size by more strictly discarding the electric noise, prior to the Crab observation.

In orbit, bias voltages for both the DSSD and APD were kept at the default value, even in the SAA. That of the CdTe-DSD was lowered once in a day when the satellite is passing through the SAA with the longest duration. This operation delays the buildup of the CdTe polarization effect significantly.<sup>21–23</sup> In the normal operation temperature, however, depolarization is not completed and a very small long-term build up remains. Because full depolarization can be done in temperature higher than  $\sim 15^{\circ}\text{C}$ , we were planning to heat up the HXI-S cold-plate to  $5^{\circ}\text{C}$  (and hence the CdTe-DSD to  $15^{\circ}\text{C}$ ) once in 1 to 6 months. When passing through the SAA, the front-end ASIC continued the normal data acquisition mode and data transfer to the satellite data recorder was stopped to save its memory size. The nine BGO units,  $^{241}\text{Am}$  source, and CR-monitor APD continued the normal operation in the SAA.

### 3.2 Basic Characteristics After Commissioning

After the commissioning operation, we first verified that all the channels are in proper status; the 1280 ch of the imager and the 11 ch of the APDs of HXI1 and HXI2 each. In Fig. 5, we present the noise level of  $2 \times 1280$  ch for the two imagers. By comparing the in-orbit value to those we observed in the on-ground measurements obtained with the same bias voltage under similar temperature, we found that all electric channels were working properly. As can be seen, the noise level is almost the same. Channels of CdTe-DSD show slightly lower noise level in orbit presumably because of a small difference in internal temperature. Thus, we concluded that the cameras had no damage at launch.

We present an  $^{241}\text{Am}$  source-tagged image and its averaged spectra of HXI1 in Fig. 6. Thanks to the time-tagging, we

obtained clear  $^{241}\text{Am}$  spectra in orbit. Using these spectra, we confirmed that the gain was unchanged before and after the launch. The energy resolution obtained was 1.0 keV (FWHM) at 13.9 keV (on layer 0, the top DSSD) and 2.0 keV (FWHM) at 59.5 keV (on layer 4, the CdTe-DSD), in both HXI1 and HXI2, also consistent with those measured on ground. The gain drift within 13 days of operation was nondetectable ( $<0.1$  keV) at 26 keV and at 59.5 keV in both detectors.

Lower thresholds for tagging the “HITPAT BGO” flag achieved in orbit are shown in Table 4. A 1-day light curve of a BGO unit and the CR-monitor APD are shown in Fig. 7. The Hitomi satellite orbits the Earth  $\sim 15$  times a day and passes the SAA 7 to 8 times. In the light curve, eight high-rate peaks coincide with the SAA passages. Because the counter of the electronics does not have sufficient data size, i.e., bit size per time bin, the count rate within or near the SAA region overflows and is not correct. Modest count rate variation apparent around the middle of the light curve is reflecting the geomagnetic cutoff rigidity (COR). The CR-monitor APD worked properly as well, showing the rate variability of (mostly) protons penetrating the BGO units and reaching near the imager. The count rate is  $\sim 1$  Hz around the normal orbit, which means  $\sim 1$  cts  $\text{s}^{-1} \text{cm}^{-2}$  CR-proton rate, and  $\sim 1$  kHz in the middle of the SAA. With this information, we will investigate the activation rate of CdTe-DSD (as well as DSSD and BGO) using a Monte Carlo simulation based on Geant4.<sup>24</sup>

Figure 8 shows the spectra of the bottom BGO unit of HXI1. To minimize the data size, only 10 min of spectra after individual SAA passages are recorded. These spectra are used to monitor the gain using the activation lines, as already mentioned in Sec. 2.2.3. Among the strongest is the 511 keV line originating from  $\beta^+$  decay in the surrounding material (such as other BGO units). Because the bottom BGO unit (BGO7) of HXI1 has the highest light yield, it has the lowest threshold of 46.5 keV. In the spectra, the Bi K-shell fluorescence lines around  $\sim 80$  keV are clearly visible.

## 4 Overview of In-Orbit Performances

### 4.1 Hard X-Ray Image and Spectra of Crab

Hitomi observed the pulsar wind nebula G21.5-0.9 as the first light target for the HXI [The Galactic binary IGR J16318-4848 was located near the edge of HXI1 FoV before HXI2 was ready, see Ref. 25]. Then, the satellite observed the isolated neutron star RX J1856-3754 to calibrate the response of the soft x-ray instruments in their lower energy-end, the data of which provides the HXI with excellent blank-sky data. Right before the incident on March 26, Hitomi observed Crab for four orbits, i.e.,  $\sim 6$  h in duration. As the satellite was in orbits with the SAA passage, which limits the usable time interval, the Crab observation provides  $\sim 6$  ks of total exposure after the appropriate data screening and dead-time correction.

The HXI1 hard x-ray image of the Crab nebula (and pulsar) in the 5- to 80-keV band is shown in Fig. 9. Using the pulse timing information, we extracted the “pulsed image” in the right panel, which shows the point-spread-function (PSF) of the HXT. The HPD of the PSF is in general consistent with those estimated from the preflight calibration. The torus of the pulsar wind nebula and the central pulsar can be seen in the hard x-ray image. Detail of the HXT in-orbit performance is presented in Matsumoto et al.<sup>3</sup> in this special section.

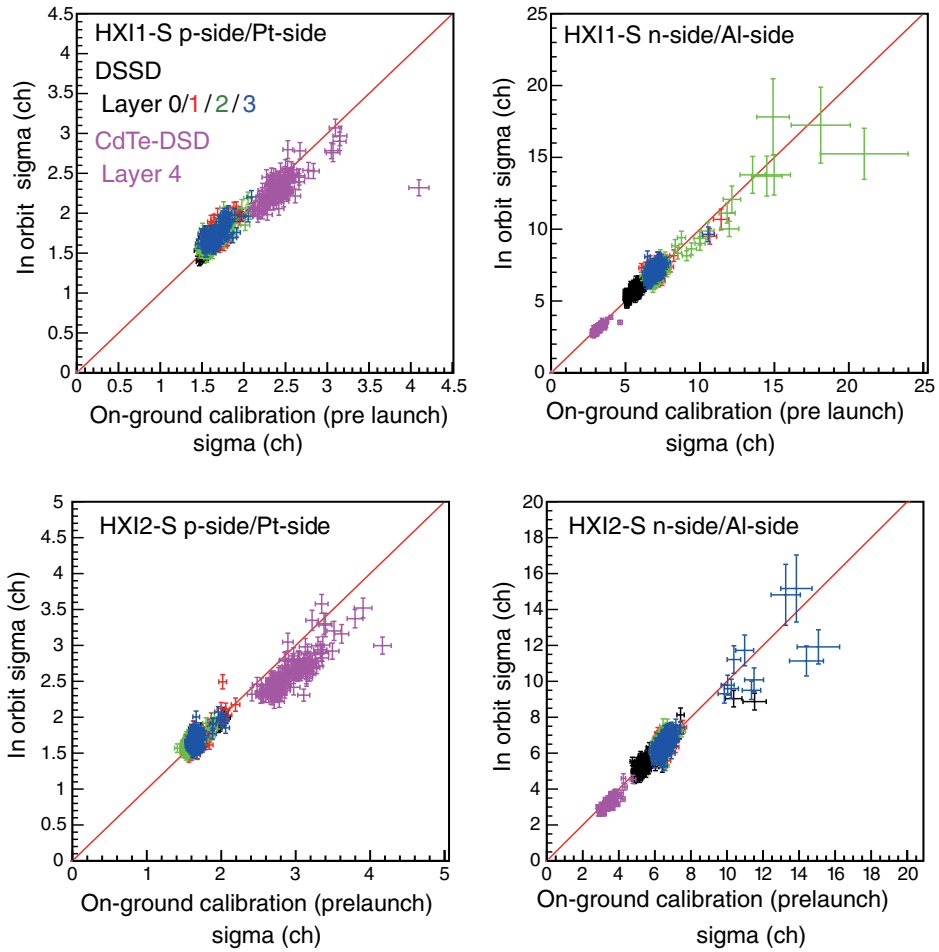


**Fig. 5** In-orbit to on-ground comparison of the noise level ( $\sigma$  in raw ADC channel) of 1280 strips each in HX11 and HX12. Typically, one ADC channel corresponds to  $\sim 0.2$  keV. The on-ground data were obtained during the thermal-vacuum test of the whole satellite system.

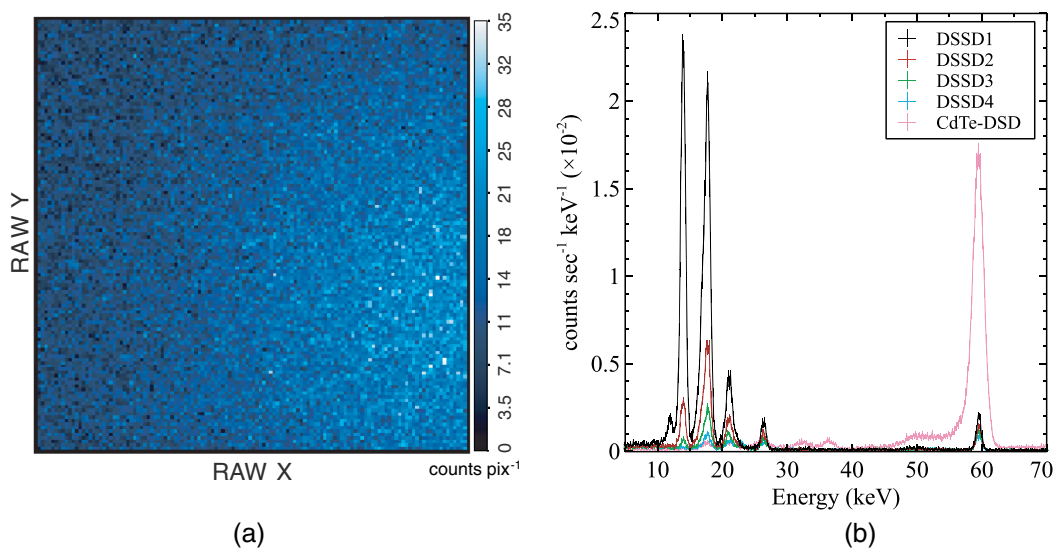


**Fig. 6** (a) In-orbit image and (b) spectra of  $^{241}\text{Am}$  tagged events of HX11. Image is written in (RAW X, RAW Y) coordinate which is in lockdown condition. Here, X and Y reflect the bottom and top side strip IDs, respectively. In the image, the  $^{241}\text{Am}$  source is located at the right side, slightly offset to the bottom. Energy resolution of DSSD events are shown to be 1.0 keV (FWHM), and that of CdTe-DSD at 59.5 keV are 2.0 keV (FWHM), both consistent with the value measured on ground.

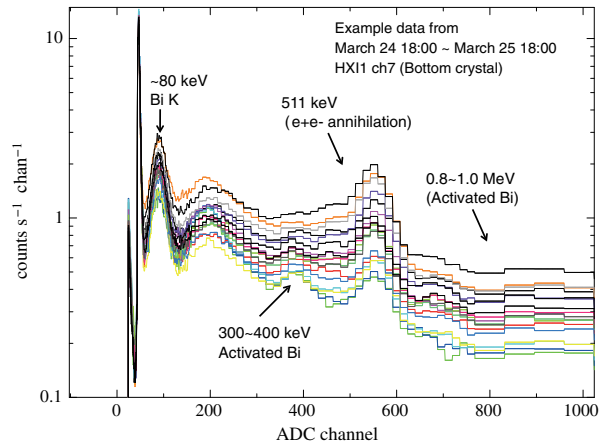
**Table 4** Lower threshold of BGO active shield’s “HITPAT BGO” flag, in units of keV.

Unit name	ID	HXI1-S	HXI2-S
Top units	1	82.7	94.5
	2	84.5	91.3
	3	86.6	100.8
	4	93.1	80.8
Bottom unit	7	46.5	52.4
Side units	8	72.0	66.7
	9	72.5	66.8
	10	66.9	76.2
	11	73.1	78.5

Detailed analysis of the HXI spectral response is summarized in Hagino et al.<sup>11</sup> Detector response at 10 to 50 keV is mostly based on ground measurements, whereas some adjustments are needed below  $\sim 10$  keV utilizing the G21.5-0.9 and the Crab spectra, which are known to follow a power law.<sup>26</sup> As shown in Hagino et al., the spectra between 5 and 80 keV can be well fitted with a power law model, with a photon index  $\Gamma = 2.107 \pm 0.002$  and normalization at 1 keV as  $N_{(1 \text{ keV})} = 10.5 \pm 0.1 \text{ photons cm}^{-2} \text{ s}^{-1} \text{ keV}^{-1}$  ( $\sim 1\%$  uncertainty in dead-time correction is included). The flux within 22 to 55 keV is calculated to be  $1.06 \times 10^{-8} \text{ erg s}^{-1} \text{ cm}^{-2}$ , which is 5% to 11% higher than those estimated from Suzaku HXD observations,<sup>26</sup> or 8% higher than those derived from the parameter recently obtained by NuSTAR’s large-offset angle observations.<sup>27</sup>

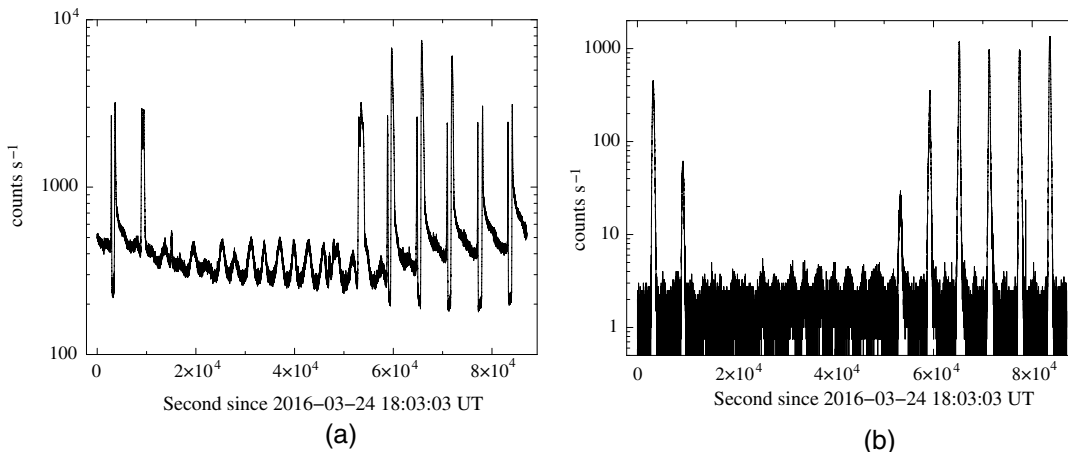
## 4.2 Background

Using the blank-sky observations, such as those of RX J1856–3754, we measured the in-orbit background that contains both the NXB and CXB. Earth occultation data were used to measure the NXB. As shown in detail in Hagino et al.,<sup>11</sup> the background consists of three major components; hard continuum component


**Fig. 8** Examples of 10 min spectra of the bottom BGO unit of the HXI1, accumulated after the SAA passages. In different colors, 16 such examples are presented. Difference of the proton counts within individual SAA passages reflect the difference in the activation spectra.

presumably originating from trapped  $\sim 100$ -keV electrons detected mainly by the top DSSD (layer 0), activation signals of CdTe clearly seen in the CdTe-DSD (layer 4), and other background components presumably from albedo neutrons and gamma-rays observed in the other three DSSDs (layers 1 to 3). Based on these background levels, we determined the energy-dependent layer selection criteria to maximize the sensitivity for dim objects, as shown in Table 5.

The left panel of Fig. 10 presents the resultant background spectra obtained after all the screening and selection. For comparison, we plotted the background of NuSTAR<sup>28</sup> FPM including the CXB (a sum of those focused from the x-ray mirror and directly incoming), downloaded from the NuSTAR proposal page and scaled to the same angular size of  $1 \text{ arcmin}^2$  (which corresponds to  $0.12$  and  $0.087 \text{ cm}^2$  in detector geometrical area for the HXI and NuSTAR, respectively). The CXB baffling, enabled by the large satellite structure of Hitomi, significantly reduces the background rate below  $\sim 10$  keV compared with those seen in NuSTAR. The layer selection technique is also contributing to reduce background below 12 keV (only layer 0) and 30 keV (layers 0 to 3). Above 30 keV, the background


**Fig. 7** (a) A one-day trigger light-curve of the bottom BGO unit of HXI1. (b) The same one of the CR monitor APD.

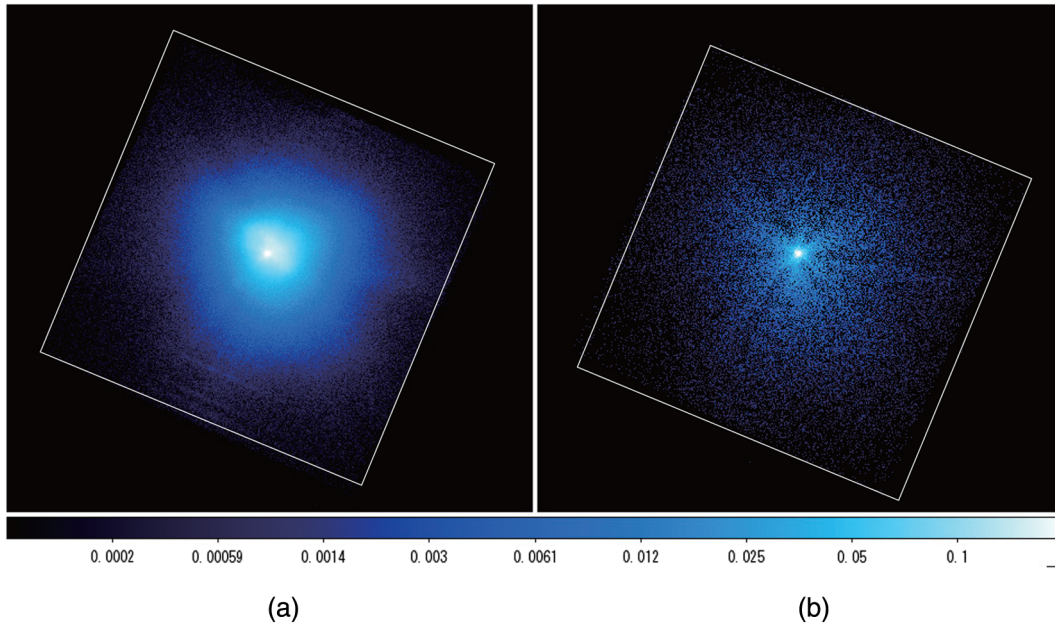


**Fig. 9** The 5 to 80 keV image of Crab obtained by HX11. (a) Time averaged and (b) pulse resolved images. Color scale is logarithmically scaled and both images have a size of  $9'.1 \times 9'.1$  arcmin<sup>2</sup>, as indicated with the white boxes. In the left panel, background is inclusive. Vignetting correction is not applied yet to both images.

**Table 5** Energy dependent layer selection criteria applied in scientific data analysis.

Energy band	5 to 12 keV	12 to 30 keV	30 to 80 keV
First DSSD	Used	Used	—
Second DSSD	—	Used	Used
Third DSSD	—	Used	Used
Fourth DSSD	—	Used	Used
CdTe-DSD	—	—	Used

is comparable or slightly (factor of  $\sim 2$ ) lower than that of the NuSTAR depending on the energy band, except for 70 to 80 keV. Even though Hitomi experiences the SAA  $\sim 8$  times a day because of the orbit inclination of 31 deg, the resultant background of CdTe including its activation is as low as those we see in NuSTAR with orbital inclination of 6 deg, which is exposed to less numbers of trapped protons (i.e., in the SAA). This is partly because of the thick BGO shield, passively stopping the SAA protons with energy  $< \sim 100$  MeV, and also the fact that CdTe-DSD of the HXI is only 0.75-mm thick, whereas the CZT of NuSTAR FPMs is 2-mm thick. (Note that CZT data analysis employs depth sensing by comparing the signals in adjacent pixels. Therefore, the effective thickness of

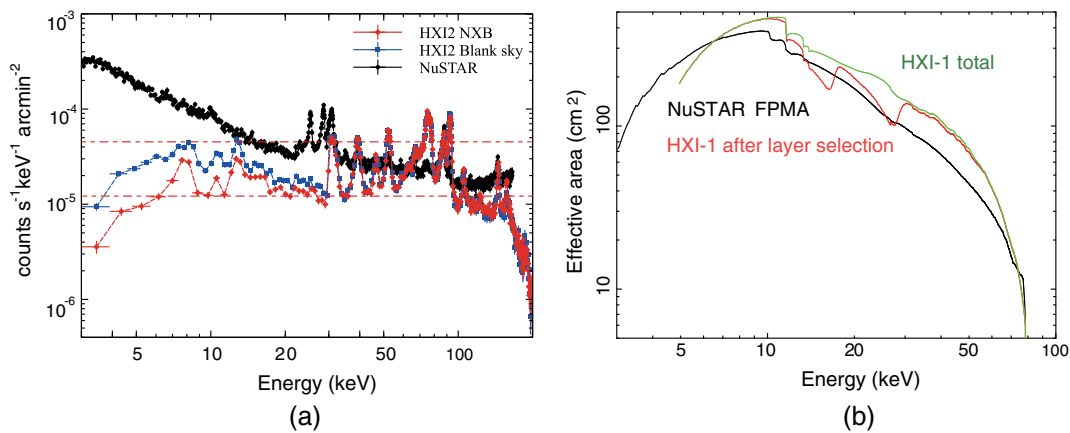


**Fig. 10** (a) HXI2 NXB and blank sky spectra compared with the NuSTAR background (black histogram). Vertical axis is scaled with the solid angle in arcmin<sup>2</sup>. Red histogram represents those of the NXB obtained during Earth occultation, whereas blue one is from the blank sky observations. The NXB-level requirement of  $1 - 3 \times 10^{-4}$  cts s<sup>-1</sup> cm<sup>-2</sup> keV<sup>-1</sup>, which can be scaled to  $1.2 - 3.6 \times 10^{-5}$  cts s<sup>-1</sup> arcmin<sup>-2</sup> keV<sup>-1</sup>, is shown for comparison as the horizontal red dot-dashed lines. (b) Effective area of HXI1 and NuSTAR, both integrated over  $4'$  radius.

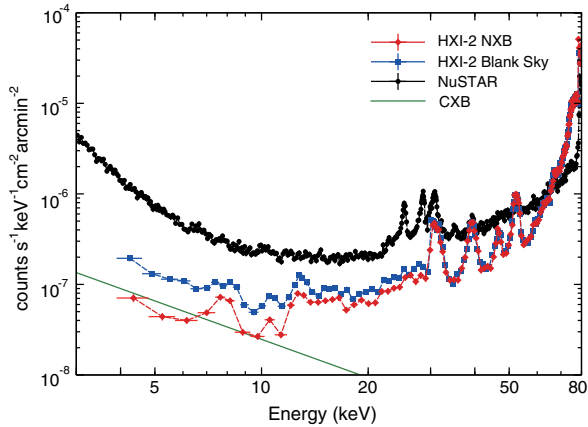


**Fig. 11** The HXI2 NXB, blank sky, and NuSTAR background scaled to their effective area and solid angle of the FoV. As a reference, a typical spectrum of CXB is also plotted.

the CZT contributing to the NuSTAR background is smaller than 2 mm.) Overall, the HXI NXB level is within 1.2 to  $3.6 \times 10^{-5}$  cts  $s^{-1}$  arcmin $^{-2}$  keV $^{-1}$ , which corresponds to the preflight requirement level of 1 to  $3 \times 10^{-4}$  cts  $s^{-1}$  cm $^{-2}$  keV $^{-1}$  scaled to the detector geometrical area.

The right panel of Fig. 10 shows the effective area of HXI before and after the energy-dependent layer selection, compared with that of NuSTAR FPMA. In general, the HXI has a little larger effective area, thanks to the longer focal length of the HXT.

Figure 11 shows the background spectra scaled to detector effective area (including optics) of the HXI and those of NuSTAR FPMA. It is clearly seen that the background-to-effective area ratio is typically 3 to 4 times better (lower) in the HXI compared with that of NuSTAR below 30 keV. Above 30 keV, the two values become almost the same, though still that of the HXI is better except for energy band above  $\sim 65$  keV. It is important to note that NuSTAR has better angular resolution of  $0'.97$  HPD<sup>28</sup> compared with that of the HXI/HXT  $1'.7$  HPD. When analyzing point sources, the background level shall be scaled with the HPD size squared, which lowers that of NuSTAR by a factor of 3.1. In other words, the background-to-effective area ratio for point sources is the same between the two instruments below  $\sim 50$  keV. In contrast, sensitivity for the diffuse source, which has an extent larger than a few arcmin, such as clusters of galaxies, directly reflects the background-to-effective area ratio shown in Fig. 11. In addition, thanks to the CXB baffling, the HXI has more stable background compared with that of NuSTAR, which is contaminated by leaking CXB and shows non-negligible time and positional dependence.<sup>29</sup> The stable and low background should have enabled the HXI to detect lower surface brightness emission than those available with NuSTAR.

## 5 Summary

The HXI combined with the HXT onboard the Hitomi x-ray satellite provides 5 to 80 keV wideband imaging spectroscopy. The HXI is designed with three important aspects to achieve low background level; well-shaped deep active shield composed of nine units of thick BGO scintillators, careful baffling of the CXB with Pb and Sn sheets taped on the HXI-S housing as well as the satellite structure itself, and five-layer stacked

semiconductor imagers composed of four DSSDs for lower energy coverage and a CdTe-DSD for higher energy coverage. By analyzing the in-flight performances of the 13 days of operation, it is shown that all signal channels have characteristics consistent with the preflight measurements. The temperature was also controlled as planned. Thus, the HXI performed mechanically and thermally well. After applying the data screening criteria shown in Hagino et al. based on satellite position on the Earth and the energy-dependent layer selection, the resultant background is  $\sim 1 - 3 \times 10^{-4}$  cts  $s^{-1}$  cm $^{-2}$  keV $^{-1}$ , meeting the preflight requirement level. This value is the lowest among the hard x-ray instruments in orbit. Our results show that the point source sensitivity is similar to that of NuSTAR and that for diffuse sources should have been better in the HXI.

## Acknowledgments

We are grateful to the whole Hitomi team; the hardware teams, the software team, as well as the operation team and the science team, for all their effort to realize the great but sadly short-lived satellite. The HXI system owes a lot to Mitsubishi Heavy Industries in its manufacturing, as well. We also note that this instrument is supported by dedicated works of many graduate and some undergraduate students from universities and research institutes in Japan and France. We acknowledge support from JSPS/MEXT KAKENHI grant numbers 24105007, 15H03639, 25287059, 24244014, and the JSPS Core-to-Core Program. All U.S. members acknowledge support through the NASA Science Mission Directorate. Stanford and SLAC members acknowledge support via DoE contract to SLAC National Accelerator Laboratory DE-AC3-76SF00515 and NASA grant NNX15AM19G. The BGO crystal and HV bias suppliers are supported from ESA. French members acknowledge support from CNES, the Centre National d'Etudes Spatiales. We thank contributions by many other companies, such as NEC, Hamamatsu Photonics, Acrorad, OKEN, Ideas, and SUPER RESIN.

## References

1. T. Takahashi et al., "The ASTRO-H mission," *Proc. SPIE* **7732**, 77320Z (2010).
2. T. Takahashi et al., "The ASTRO-H (Hitomi) x-ray astronomy satellite," *Proc. SPIE* **9905**, 99050U (2016).
3. H. Matsumoto et al., "In orbit performance of the hard x-ray telescope (HXT) on board the Hitomi (ASTRO-H) satellite," *J. Astron. Telesc., Instrum., Syst.* **4**(1), 011212 (2017).
4. Y. Fukazawa et al., "Development of low-noise double-sided silicon strip detector for cosmic soft gamma-ray Compton camera," *Nucl. Instrum. Methods Phys. Res., Sect. A* **541**(1), 342–349 (2005).
5. S. Takeda et al., "Development of double-sided silicon strip detectors (DSSD) for a Compton telescope," *Nucl. Instrum. Methods Phys. Res., Sect. A* **579**(2), 859–865 (2007).
6. S. Watanabe et al., "High energy resolution hard x-ray and gamma-ray imagers using CdTe diode devices," *IEEE Trans. Nucl. Sci.* **56**, 777–782 (2009).
7. H. Tajima et al., "Performance of a low noise front-end ASIC for Si/CdTe detectors in Compton gamma-ray telescope," *IEEE Trans. Nucl. Sci.* **51**, 842–847 (2004).
8. T. Takahashi et al., "Hard x-ray detector (HXD) on board Suzaku," *Publ. Astron. Soc. Jpn.* **59**, S35–S51 (2007).
9. M. Kokubun et al., "In-orbit performance of the hard x-ray detector on board Suzaku," *Publ. Astron. Soc. Jpn.* **59**, S53–S76 (2007).
10. K. Yamaoka et al., "Design and in-orbit performance of the Suzaku wide-band all-sky monitor," *Publ. Astron. Soc. Jpn.* **61**(sp1), S35–S53 (2009).

11. K. Hagino et al., “In-orbit performance and calibration of the hard x-ray imager (HXI) onboard Hitomi,” *J. Astron. Telesc. Instrum. Syst.* **4**(2), 021409 (2018).
12. M. Kokubun et al., “The hard x-ray imager (HXI) for the ASTRO-H mission,” *Proc. SPIE* **8443**, 844325 (2012).
13. T. Saito et al., “Development of high performance avalanche photodiodes and dedicated analog systems for HXI/SGD detectors onboard the Astro-H mission,” *Nucl. Instrum. Methods Phys. Res., Sect. A* **699**, 230–234 (2013).
14. H. Noda et al., “Thermal design of the hard x-ray imager and the soft gamma-ray detector onboard ASTRO-H,” *Proc. SPIE* **9144**, 91445E (2014).
15. G. Sato et al., “The Si/CdTe semiconductor camera of the ASTRO-H hard x-ray imager (HXI),” *Nucl. Instrum. Methods Phys. Res., Sect. A* **831**, 235–241 (2016).
16. K. Nakazawa et al., “Hard x-ray imager for the NeXT mission,” *Proc. SPIE* **6266**, 62662H (2006).
17. Y. Terada et al., “The time assignment system and its performance aboard the Hitomi satellite,” *J. Astron. Telesc. Instrum. Syst.* **4**(1), 011206 (2017).
18. Y. Fukazawa et al., “Modeling and reproducibility of Suzaku HXD PIN/GSO background,” *Publ. Astron. Soc. Jpn.* **61**, S17–S33 (2009).
19. M. Sasano et al., “Geometry dependence of the light collection efficiency of BGO crystal scintillators read out by avalanche photo diodes,” *Nucl. Instrum. Methods Phys. Res., Sect. A* **715**, 105–111 (2013).
20. M. Ohno et al., “Development and verification of signal processing system of BGO active shield onboard Astro-H,” *Proc. SPIE* **9144**, 91445G (2014).
21. G. Sato et al., “Study of polarization phenomena in Schottky CdTe diodes using infrared light illumination,” *Nucl. Instrum. Methods Phys. Res., Sect. A* **652**(1), 149–152 (2011).
22. D. Maier et al., “A laboratory test setup to study the stability of operation of the CdTe detectors within Astro-H HXI,” *Proc. SPIE* **9905**, 990542 (2016).
23. D. Maier et al., “Long-term test of a stacked CdTe mini-HXI setup,” *Nucl. Instrum. Methods Phys. Res., Sect. A* (2017), in press.
24. H. Odaka et al., “Modeling of proton-induced radioactivation background in hard x-ray telescopes: Geant4-based simulation and its verification by Hitomi’s measurement in a low Earth orbit,” *Nucl. Instrum. Methods Phys. Res., Sec. A* **891**, 92–105 (2018).
25. Hitomi-collaboration et al., “Glimpse of the highly obscured HMXB IGR J16318–4848 with Hitomi,” PASJ (2018), in press.
26. T. Kouzu et al., “Spectral variation of hard x-ray emission from the crab nebula with the suzaku hard x-ray detector,” *Publ. Astron. Soc. Jpn.* **65**(4), 74 (2013).
27. K. K. Madsen et al., “Measurement of the absolute crab flux with NuSTAR,” *Astrophys. J.* **841**, 56 (2017).
28. F. A. Harrison et al., “The nuclear spectroscopic telescope array (NuSTAR) high-energy x-ray mission,” *Astrophys. J.* **770**(2), 103 (2013).
29. D. R. Wik et al., “NuSTAR observations of the bullet cluster: constraints on inverse compton emission,” *Astrophys. J.* **792**, 48 (2014).

**Kazuhiro Nakazawa** received his BS and MS degrees in physics from the University of Tokyo in 1996 and 1998, respectively, and his PhD in physics in 2001. He was a lecturer at the University of Tokyo when this work was performed, and now he is an associate professor at Nagoya University.

**Goro Sato** received his BS and MS degrees in physics from the University of Tokyo in 2000 and 2002, respectively, and his PhD in physics in 2006. Currently, he is an associate senior engineer at JAXA.

**Motohide Kokubun** received his BS and MS degrees in physics from the University of Tokyo in 1996 and 1998, respectively, and his PhD in physics in 2001. Currently, he is an associate professor at ISAS/JAXA.

Biographies for the other authors are not available.